

# Structure and Composition of Molecular Clouds with CN Zeeman Detections I: W3OH

Nicholas S. Hakobian and Richard M. Crutcher

*University of Illinois at Urbana-Champaign*

*1002 W. Green Street, Urbana IL*

nhakobi2@astro.illinois.edu, crutcher@illinois.edu

## ABSTRACT

We have carried out a multi-species study of a region which has had previous measurements of strong magnetic fields through the CN Zeeman effect in order to explore the relationship between CN and  $\text{N}_2\text{H}^+$ , both of which have evidence that they remain in the gas phase at densities of  $10^5 - 10^6 \text{ cm}^{-3}$ . To achieve this we map the 1 arcmin<sup>2</sup> region around the UCHII region of W3(OH) using the Combined Array for Millimeter-wave Astronomy (CARMA). Approximately 105 hours of data were collected in multiple array configurations to produce maps with an effective resolution of  $\sim 2.5''$  at high signal-to-noise in CN,  $\text{C}^{18}\text{O}$ , HCN,  $\text{HCO}^+$ ,  $\text{N}_2\text{H}^+$ , and two continuum bands (91.2 GHz and 112 GHz). These data allow us to compare tracer molecules associated with both low and high density regions to infer gas properties. We determine that CARMA resolves out approximately 35% of the CN emission around W3(OH) when compared with spectra obtained from the IRAM-30 meter telescope. The presence of strong absorption lines towards the continuum source in three of the molecular transitions infers the presence of a cold, dark, optically thick region in front of the continuum source. In addition, the presence of high-velocity emission lines near the continuum source shows the presence of hot clumpy emission behind the continuum source. These data determine that future high-resolution interferometric CN Zeeman measurements which cannot currently be performed (due to technical limitations of current telescopes) are feasible. We confirm that CN is indeed a good tracer for high density regions; with certain objects such as W3(OH) it appears to be a more accurate tracer than  $\text{N}_2\text{H}^+$ .

## 1. Introduction

The measurement of magnetic fields harbor several difficulties due to the fact that they are a vector quantity. In order to measure the absolute magnitude and direction of the magnetic field, it is necessary to sample the two components in the plane of the sky and the line-of-sight component. While dust polarization can measure the direction of a magnetic field in the plane of the sky, the line-of-sight component intensity can be directly measured. This is accomplished

through the detection of the normal Zeeman effect which occurs when an atom or molecule is in the presence of a magnetic field. Most transitions have a Zeeman splitting factor that is too small to measure unless in dense, spatially-compact environments with exceedingly large magnetic field strengths. However, HI, OH, and CN have splitting factors that are large enough to measure the weaker magnetic fields that are expected around sites of active star formation in molecular clouds. The CN  $N = 1-0$  transition has seven strong hyperfine components (Table 1) that have a large distribution of Zeeman splitting factors. The two strongest hyperfine components, with relative strengths of 27 and 10 respectively, also have large splitting factors.

Falgarone et al. (2008) surveyed 14 molecular cloud cores and measured the line-of-sight magnetic field strength using the CN Zeeman effect. The strongest magnetic field detected was  $1.10 \pm 0.33$  mG towards the Ultra-Compact HII (UCHII) region of W3(OH) (Hoare 2004), a high mass star formation site in the W3 molecular cloud complex. For these measurements, Falgarone et al. (2008) used the IRAM 30-meter telescope. Due to the relatively large beam size of the IRAM-30 meter telescope ( $23''$  or 46,000 AU in diameter at the 2 kpc distance (Hachisuka et al. 2006) of W3(OH)), only very limited mapping to find the emission peak was performed. From these data, it is not possible to determine the structure of the magnetic field or which material the field is associated with.

W3(OH) contains a high-mass O star and has been extensively studied over the years since the discovery of several OH maser sites within it (Raimond & Eliasson 1969). A star forming region  $6''$  east of W3(OH) was later discovered by Turner & Welch (1984) in HCN. This smaller region was also studied for maser activity and found to contain several  $H_2O$  masers (Wynn-Williams et al. 1972). While this second source was initially not observed in the continuum, with the development of more sensitive instruments, it was eventually detected in dust continuum studies (Wilner et al. 1995; Wyrowski et al. 1997). Within the last few years, further high resolution studies with instruments such as BIMA have led to the detection of multiple dense cores believed to be sites of active star formation within the Turner-Welch Object (Chen et al. 2006).

In order to determine the spatial distribution of the magnetic field, an understanding of the CN gas is needed. There is some question, however, as to the exact physical conditions that CN traces. Hily-Blant et al. (2008) used the IRAM 30-m telescope to conclude that CN in prestellar cores stays in the gas phase at densities close to  $10^6 \text{ cm}^{-3}$  and can serve as a kinematic tracer of high density gas. They compared their CN maps with  $N_2H^+$ , another high density tracer, and found the results to be in good agreement. Therefore, it is expected that the measured magnetic field strength derived from CN measurements would be in gas that is associated with high density regions of active star formation. However, before detailed conclusions can be drawn from these magnetic field measurements, a high angular resolution study of the CN gas distribution is required. An ideal instrument for this is an interferometer such as CARMA, as its high spatial resolution and ability to sample baselines as short as 6m allow us to sample material both spatially compact and widespread.

Table 1. CN Hyperfine Components

Molecule	Transition	$\nu$ (MHz)	Z (Hz/ $\mu$ G) <sup>a</sup>	RI <sup>b</sup>
CN	N=1 – 0 J= $\frac{1}{2}$ – $\frac{1}{2}$ F= $\frac{1}{2}$ – $\frac{1}{2}$	113123.337	– <sup>c</sup>	1
CN	N=1 – 0 J= $\frac{1}{2}$ – $\frac{1}{2}$ F= $\frac{1}{2}$ – $\frac{3}{2}$	113144.192	2.18	8
CN	N=1 – 0 J= $\frac{1}{2}$ – $\frac{1}{2}$ F= $\frac{3}{2}$ – $\frac{1}{2}$	113170.528	-0.31	8
CN	N=1 – 0 J= $\frac{1}{2}$ – $\frac{1}{2}$ F= $\frac{3}{2}$ – $\frac{3}{2}$	113191.317	0.62	10
CN	N=1 – 0 J= $\frac{3}{2}$ – $\frac{1}{2}$ F= $\frac{3}{2}$ – $\frac{1}{2}$	113488.140	2.18	10
CN	N=1 – 0 J= $\frac{3}{2}$ – $\frac{1}{2}$ F= $\frac{5}{2}$ – $\frac{3}{2}$	113490.982	0.56	27
CN	N=1 – 0 J= $\frac{3}{2}$ – $\frac{1}{2}$ F= $\frac{1}{2}$ – $\frac{1}{2}$	113499.639	0.62	8
CN	N=1 – 0 J= $\frac{3}{2}$ – $\frac{1}{2}$ F= $\frac{3}{2}$ – $\frac{3}{2}$	113508.944	1.62	8
CN	N=1 – 0 J= $\frac{3}{2}$ – $\frac{1}{2}$ F= $\frac{1}{2}$ – $\frac{3}{2}$	113520.414	– <sup>c</sup>	1

<sup>a</sup>Z is the Zeeman Splitting Factor for each hyperfine component of CN.

<sup>b</sup>RI is the relative intensity of each component.

<sup>c</sup>The Z's for these hyperfine components were not calculated due to their low RI.

References. — Falgarone et al. 2008

## 2. CARMA Observations

With CARMA (Bock et al. 2006) it is possible to achieve a resolution of approximately  $2.5''$  by combining maps generated with the C, D, and E arrays. By using three different array configurations, we have the ability to probe small scale structure while retaining the ability to image large scale features that would otherwise be resolved out in the C and D arrays. CARMA currently does not have polarization capability and therefore cannot perform magnetic field measurements; however, by mapping these regions at high resolution we can gain crucial information as to the structure of the regions that are being sampled by the IRAM observations. To assist with this, we use the advanced features of CARMA’s correlator to sample several spectral lines simultaneously, so we can compare the structure of the CN emission with emission of other well studied tracer molecules. We will also gain information on which regions are possible to map in the Zeeman effect at high resolution and for long integration times with an instrument capable of making dual-polarization measurements, when such an interferometer array becomes available.

The CARMA observations began in Spring 2007 and were completed in Fall of 2009. About 66 hours of observing time was used to map a  $1 \text{ arcmin}^2$  region around W3(OH). This time was used to observe the following molecular tracers: CN,  $\text{C}^{18}\text{O}$ ,  $\text{N}_2\text{H}^+$ , HCN, and  $\text{HCO}^+$  (Table 2). Due to the design of the CARMA correlator and the relatively large frequency range within the 3-mm band that these tracers span, the measurements had to be performed in two separate tracks: one for CN and  $\text{C}^{18}\text{O}$ , and a second for  $\text{N}_2\text{H}^+$ , HCN, and  $\text{HCO}^+$ . Approximately 50 hours (Table 3) was spent for the CN band and 16.2 hours was spent for the  $\text{N}_2\text{H}^+$  band (not counting additional time spent in B array, discussed below). In order for us to reach our signal to noise goal, the tracks containing  $\text{N}_2\text{H}^+$  required much less observing time. Table 3 shows the observing array details. Our pointing center is located on the continuum source, an ultra-compact HII region, located at: 02:27:03.7 RA, +61:52:25 DEC (J2000). This is slightly offset from the IRAM pointing position.

We produced maps for 3-mm lines of CN,  $\text{C}^{18}\text{O}$ ,  $\text{N}_2\text{H}^+$ , HCN, and  $\text{HCO}^+$  at a resolution of approximately  $2.5''$ . The composite CARMA primary beam at half power at this frequency is slightly more than  $60''$  in diameter, reflected in our maps, which are  $64''$  on a side. Since baselines as short as 6m are included, the maps are sensitive to structure smaller than about  $90''$ , so that the spatial dynamic range is almost 40:1. At the distance of W3(OH) (2 kpc), this means the maps are about 0.62 pc across, and the resolution is about 0.024 pc or 5,000 AU. For all of the spectral line observations, we used the 8 MHz spectral line mode, which for CN ( $\text{N}_2\text{H}^+$ ) provides a velocity coverage of  $\sim 21 \text{ km s}^{-1}$  ( $\sim 25.8 \text{ km s}^{-1}$ ) and a resolution of  $0.335 \text{ km s}^{-1}$  ( $0.415 \text{ km s}^{-1}$ ). The other transitions have similar coverages and resolutions which vary depending on their rest frequency. The large velocity coverage is necessary to simultaneously image several hyperfine components while still maintaining a high spectral resolution. Our data also contains two 500 MHz continuum bands in each track giving us four separate continuum windows between 88 GHz and 113 GHz. These continuum maps, while having a lower spatial resolution than some previously published maps of W3(OH) (Chen et al. 2006), have a significantly higher signal-to-noise ratio.

Table 2. Observed Transitions

Molecule	Transition	$\nu$ (MHz)
HCN	N=1 – 0 F=1 – 1	88630.415
HCN	N=1 – 0 F=2 – 1	88631.847
HCN	N=1 – 0 F=0 – 1	88633.936
HCO <sup>+</sup>	N=1 – 0	89188.526
N <sub>2</sub> H <sup>+</sup>	N=1 – 0 F <sub>1</sub> =1 – 1 F=0 – 1	93171.621
N <sub>2</sub> H <sup>+</sup>	N=1 – 0 F <sub>1</sub> =1 – 1 F=2 – 2	93171.917
N <sub>2</sub> H <sup>+</sup>	N=1 – 0 F <sub>1</sub> =1 – 1 F=1 – 0	93172.053
N <sub>2</sub> H <sup>+</sup>	N=1 – 0 F <sub>1</sub> =2 – 1 F=2 – 1	93173.480
N <sub>2</sub> H <sup>+</sup>	N=1 – 0 F <sub>1</sub> =2 – 1 F=3 – 2	93173.777
N <sub>2</sub> H <sup>+</sup>	N=1 – 0 F <sub>1</sub> =2 – 1 F=1 – 1	93173.967
N <sub>2</sub> H <sup>+</sup>	N=1 – 0 F <sub>1</sub> =0 – 1 F=1 – 2	93176.265
C <sup>18</sup> O	N=1 – 0	109782.176
CN	N=1 – 0 J= $\frac{3}{2}$ – $\frac{1}{2}$ F= $\frac{3}{2}$ – $\frac{1}{2}$	113488.140
CN	N=1 – 0 J= $\frac{3}{2}$ – $\frac{1}{2}$ F= $\frac{5}{2}$ – $\frac{3}{2}$	113490.982

Table 3. W3OH Observation Lengths

Array Config	CN, C <sup>18</sup> O	HCN, HCO <sup>+</sup> , N <sub>2</sub> H <sup>+</sup>	Resolution
C	28.0h	7.4h	1.5''
D	8.1h	4.3h	5.0''
E	11.0h	4.5h	10.0''
B	30h	12h	~ 0.7''

MIRIAD was used for data reduction, specifically with the modifications for use with CARMA. Due to the nature of CARMA, with 3 distinct primary beams, the data were reduced as a mosaic data set with a common pointing center. Passband calibration was performed on all tracks by utilizing the CARMA system noise source. Even though suitable passband calibrators were observed for every track, it was decided that better passband solutions could be obtained from the noise source. Flux calibration was performed on each individual track with a 15 minute observation of MWC349, Mars, or Uranus, whichever was best suitable at observation time as the intrinsic flux of these sources is very well modeled. Since our data were obtained over such a long period of time, the flux of our primary phase calibrator varied significantly. We determine the flux of the phase calibrator through a bootstrapping process by which our flux calibrator measurements are used to calibrate the flux scale for the point source phase calibrator. It is estimated that there is an inherent 20% error with this flux calibration technique. Phase calibration was performed primarily on 0359+509 with a secondary calibrator 0102+584, used if the primary was not visible for a significant portion of the track. The primary phase calibrator had an averaged bootstrapped flux of 6.16 Jy over 10 tracks obtained over a period of 20 months. The flux steadily increased from 3.9 Jy to 10.7 Jy over this time. In order to corroborate the flux measurements we compared our data with that obtained by the CARMA flux calibration commissioning task. This independent flux measurement of 0359+509 is 9.83 Jy (from Fall 2009), consistent with our measurement of 10.7 Jy from the same time period, assuming the 20% uncertainty mentioned above. Gain and phase calibration was performed with the *gfiddle* routine which fits an n-th order polynomial to the phase measurements on the phase calibrator. This method was chosen in contrast to the more widely used *selfcal* technique (on the calibrator) due to the weak signal strength of some of our spectral lines. However the benefits of this technique over the *selfcal* technique have not been shown; overall this technique may not have any net advantage. It may be possible to gain an increased signal to noise by performing self-calibration on W3OH itself, as the continuum source in the center of the map remains unresolved in all of the array configurations and is bright enough to perform phase calibration in the spectral channels. However, the absolute position of the phase center of the map is not retained and flux calibration is not guaranteed to succeed. These details are described in detail below in the description of our B-array data.

Since CARMA is composed of two types of telescopes of differing sizes, we have to handle the fact that we have multiple primary beam types associated with our data. CARMA has both 10-meter and 6-meter dishes which form 3 effective primary beams with the same phase center: one for the pairing of 10-meter to 10-meter dish, one for 6-meter to 6-meter, and a third of 10-meter to 6-meter. At the CN line frequency the 6-meter primary beam half power beam width (HPBW) is  $\sim 111''$ , the 10-meter HPBW is  $\sim 66''$  (at the  $N_2H^+$  frequency of 93 GHz, these HPBWs are  $135''$  and  $81''$ , respectively), while the 6m-10m primary beam size is in between that of the other two. We conservatively constrained our maps to  $\sim 1$  arcmin<sup>2</sup> in order to easily compare the other maps with the CN data. The restoring beam size is calculated by fitting the dirty beam with a Gaussian beam. This is the effective resolution of a map, and is the value quoted in all of our figures.

Image conversion from the UV-dataset into the spatial domain was performed by the MIRIAD routine *invert*. System temperature weighting was used to properly downweight data taken at low elevation or in the unlikely event that data were improperly flagged. The CARMA control system has an intricate flagging mechanism that operates if one of many error conditions are met including: telescope tracking errors, pointing errors, receiver problems (dewar temperature, LO frequency, etc), system temperature, and other computer or correlator errors that could hinder data integrity. All data were additionally inspected for extreme system temperatures, unphysical antenna gains, time regions without converging phase solutions, and poor weather conditions that could influence the quality of the data. In a few cases (usually in older tracks before some automated flagging conditions were introduced) data that contained systematic errors were manually flagged. This additional flagging increased the signal-to-noise of these few tracks by a factor of 2-3. In the *invert* step, we weighted our UV data using a Briggs visibility weighting robustness parameter of 1 (Briggs et al. 1999), which provides a slightly increased signal-to-noise ratio over uniform weighting at the expense of a larger synthesized beam size. The relatively weak CN emission prompted the weighting of data in this manner. Since we are detecting low-level emission we did not want large sidelobes to obscure the detections. If we changed the weighting more towards Natural weighting, we could have reduced the noise level further; however, the beam size would be significantly larger and we would be affected by significant sidelobes. Cleaning was performed with the MIRIAD task *mosstdi*, the mosaic version of the standard Steer clean routine. We used a multi-step cleaning technique in order to prevent under-cleaning the source. A small number of clean iterations was performed in order to remove large scale beam patterns while leaving much of the low intensity source features uncleaned. From this initial clean, we ran the MIRIAD task *restor* which used the clean data to produce a map without beam effects. We used the average off-line noise level in this map to limit how much flux was cleaned from a second iteration of *mosstdi* and to prevent overcleaning. This second stage *mosstdi* iteration was followed by another *invert* step to produce a final, deep cleaned map. In theory, this process can be repeated ad infinitum, however, if the noise level calculated in the first step is accurate, and the maximum number of cleaning iterations is large enough such that we are guaranteed to clean down to the noise level, this two step process is adequate.

### 3. Results

#### 3.1. CN

Figure 1 shows integrated line maps of the five species, while Figure 2 shows channel maps. The continuum source was removed from the spectral line maps by averaging several off-line channels together and subtracting that from each individual channel. Towards the continuum source, we see three of the species strongly in absorption. Besides the Turner-Welch object and the continuum source, there are two other regions that are notable in CN. The western side of the map contains very diffuse CN emission, while the eastern side of the map shows a compact and complex CN emission

source. In order to compare the CARMA CN data with the IRAM CN data (Falgarone et al. 2008), we also generated a map where the CARMA channel data were convolved with a  $23''$  Gaussian beam, effectively smoothing the CARMA data to match the IRAM resolution (see §4.2). By comparing these maps, there is evidence that both spectra are dominated by diffuse emission.

Compared to the other molecules, the CN emission appears to be diffuse but “clumpy.” Under closer scrutiny, it is much more complex. Our 8 MHz spectral window is centered at 113.490982 GHz, the frequency of CN’s strongest hyperfine component. This frequency and window size was chosen to allow us to simultaneously image a second hyperfine component of the CN N=1-0 transition at 113.488 GHz in the same spectral window. These two hyperfine components are separated by  $7.9 \text{ km s}^{-1}$ . Since this window covers approximately  $21 \text{ km s}^{-1}$  of velocity space, we expect to fully resolve and image both lines. Multiple velocity components in the image make it difficult to determine which hyperfine component some emission belongs to. However, we have been able to identify at least three distinct velocity components, representing separate regions around W3(OH) (Figure 3).

The north-west and south-west components appear to be very diffuse. They are centered at approximately  $-47.25 \text{ km s}^{-1}$  and  $-44.5 \text{ km s}^{-1}$ , respectively. It is difficult to completely isolate these two velocity components due to blending and overlap of the hyperfine lines. The maps in Figure 3 reflect some of this “blending.” It occurs because the second hyperfine component of one velocity partially overlaps the primary hyperfine component of the other velocity. For example, the second and third maps in Figure 3 are cross-contaminated. This is easily visible when the positions of the emission in the two maps are compared; they have a significant spatial overlap region.

The north-eastern component is more complex. In addition to containing diffuse emission, multiple denser clumps are visible. The significance of some of these clumps are not clear from the integrated line map. Between the larger southernmost clump and the smaller, northern clump are a string of small, presumably unresolved clumps only seen in a single channel each. When viewing an averaged line map, many of these features are spatially smoothed and are not prominent (as in Figure 3). The densest portions of this region are concentrated in two lobes, not unlike the typical signature of an outflow. Figure 4 shows channel maps of the 15 channels around the strongest hyperfine component. There does not appear to be any blending as was seen in the south west component, so we are confident that this channel map is not contaminated. An averaged contour plot (Figure 5) shows the physical comparison between the two “lobes” of the emission. The top (red shifted) lobe is averaged from the six channels from  $-47.6 \text{ km s}^{-1}$  to  $-49.2 \text{ km s}^{-1}$ , while the bottom (blue shifted) lobe is averaged from the six channels from  $-49.2 \text{ km s}^{-1}$  to  $-50.8 \text{ km s}^{-1}$ . While this does have the signature of a typical outflow, it is not accompanied by any coincident emission from any of the other species, nor is there any accompanying IR emission source visible in publicly available IR catalogs. Due to the extent of the low level emission around the whole region, and lack of evidence of an outflow generating source, it is more likely that this is not an outflow, but rather bulk rotation of a clump of gas.



### 3.2. HCN, HCO<sup>+</sup>, C<sup>18</sup>O

The maps for HCN, HCO<sup>+</sup>, C<sup>18</sup>O all appear to be tracing the same material, which does not coincide with either the CN or N<sub>2</sub>H<sup>+</sup> emission (see Figures 6-8 for channel maps). However, the peak position of these spectral lines coincides with the HCN detection of the Turner-Welch object first reported in Turner & Welch (1984). At 2.5'' resolution we do not appear to be resolving the object; previous high resolution (sub-arcsecond) studies have been conducted in order to resolve this object in the continuum (Chen et al. 2006), which resulted in the detection of multiple cores. Previous HCO<sup>+</sup> studies (Wink et al. 1994) had similar spatial resolution to our data, however, our data has significantly better signal-to-noise and samples material that was resolved out in the previous study. In the HCO<sup>+</sup> spectrum of the Turner-Welch object, a weak, secondary velocity component at -44 km s<sup>-1</sup> is visible (Fig. 9). This velocity component is not reported in any previous studies. The HCN spectra towards the Turner-Welch object shows an unexpected peak at an apparent velocity of -39 km s<sup>-1</sup> (Fig. 9); comparing relative positions of these two peaks, the anomalous HCN peak would be the F=0-1 transition of a secondary velocity component at -44 km s<sup>-1</sup>. The other hyperfine lines from this velocity component are being masked by the hyperfine lines from the primary velocity component. This can only happen if the separation between the hyperfine lines is approximately the separation between the two velocity components. The C<sup>18</sup>O line may also show this secondary component, however, it cannot be confirmed due to the relatively low SNR of the C<sup>18</sup>O emission.

The C<sup>18</sup>O map does not show any absorption towards the continuum source, unlike HCN, HCO<sup>+</sup>, and CN. This is consistent with observations done by Wink et al. (1994), in which they surmised that the line excitation temperature of HCO<sup>+</sup> is significantly lower than the kinetic temperature of 90 K; but the C<sup>18</sup>O excitation temperature is not low enough to produce absorption. However, our observed absorption in other lines is significant and can yield information about the regions around the continuum source. The HCO<sup>+</sup> spectra, seen in absorption (Figure 9), looks similar to an inverse P-Cygni profile which could indicate an expanding shell-like structure or a strong stellar wind. The multiple hyperfine components of HCN make it difficult to tell which gas is causing the absorption; however, it has the same central velocity and line width as the HCO<sup>+</sup> absorption indicating that both features are being generated from the same region. The CN absorption also appears to have similar spectral features as HCN; however the red-shifted CN emission feature is at a level of less than 1σ of the noise level, and cannot be considered as a positive detection.

Another notable feature of the continuum absorption lines is their shape. There is a double trough shape seen in HCO<sup>+</sup>, the strongest hyperfine component of HCN, and in CN (these spectra are centered on the strongest hyperfine component). There is also some evidence of this feature in the other hyperfine components; however they are weaker and, as a result, noisier. According to the results of Wink et al. (1994), within the UCHII region of W3(OH) there is an embedded O7 star. It is very likely that W3(OH) is a region surrounding a bright massive star embedded in a dense cloud with a strong solar wind clearing out the region around the star. In looking at a

velocity moment map in  $\text{HCO}^+$  ( $\text{HCO}^+$  was chosen due to its lack of hyperfine components and contamination), there appears to be an East-West velocity gradient on the order of  $3 \text{ km s}^{-1}$ . Since  $\text{W3(OH)}$  is unresolved in these maps, higher resolution data of  $\text{W3(OH)}$  are required to quantify and describe this effect (see below).

### 3.3. $\text{N}_2\text{H}^+$

Figure 10 shows  $\text{N}_2\text{H}^+$  channel maps. If  $\text{N}_2\text{H}^+$  were tracing the same dense material as CN, we would expect to see very similar emission (and absorption) spectra. Most notable is the lack of an absorption feature towards the continuum source, or alternatively, of any emission in  $\text{N}_2\text{H}^+$  at the continuum position. Also, the rotation feature in CN noted above is not seen in  $\text{N}_2\text{H}^+$ . The  $\text{N}_2\text{H}^+$  emission appears to be concentrated in the south western region of the map, roughly coincident with one of the velocity components of CN; however, this is where the similarity ends. In the  $\text{N}_2\text{H}^+$  spectra (Figure 9), only 3 peaks appear when there are 7 hyperfine lines within our window. The central peak, at about  $-47.5 \text{ km s}^{-1}$ , contains 3 hyperfine components which, having only  $0.487 \text{ MHz}$  ( $1.56 \text{ km s}^{-1}$ ) between them, are blended together. The peak centered at  $-42.5 \text{ km s}^{-1}$  contains another three hyperfine components whose transition frequencies all lie within  $0.432 \text{ MHz}$  ( $1.39 \text{ km s}^{-1}$ ) and would also appear blended. The last hyperfine component is seen at  $-56 \text{ km s}^{-1}$  and is the only one that is not blended. Our  $\text{N}_2\text{H}^+$  map contains some similarities to the ammonia ( $\text{NH}_3$ ) map presented by Wilson et al. (1993) and Tieftrunk et al. (1998). The major difference between the two is the lack of  $\text{N}_2\text{H}^+$  emission around the Turner-Welch object. The major similarity comes from an east-west elongated clump present in the northeast corner of both the  $\text{N}_2\text{H}^+$  emission and the  $\text{NH}_3$  emission. This stands out since none of the other molecules show any sign of emission from this region. The closest emission is the north lobe of the possible CN outflow. It is unclear if these regions are related.

It is possible that the regions of CN emission much more closely matches the regions of  $\text{N}_2\text{H}^+$  than is readily apparent, even though the spatial peaks do not coincide. Since CN is significantly weaker than  $\text{N}_2\text{H}^+$ , it is possible that emission, particularly in the lower west side of the map that is detectable in  $\text{N}_2\text{H}^+$ , is significantly below the noise threshold in CN. To emphasize this fact, which may not be noticeable in the individual channel maps, we constructed a channel map with 20% contours from all five detected species (Fig. 11). Most noticeable in the  $-48 \text{ km s}^{-1}$  and  $-47 \text{ km s}^{-1}$  panels, CN (with several other of the species) does seem to trace much of the  $\text{N}_2\text{H}^+$  emission. In the  $-51 \text{ km s}^{-1}$  and  $-50 \text{ km s}^{-1}$  panels, it appears that the  $\text{N}_2\text{H}^+$  emission borders on the regions with emission in the other species. If we assume that the two molecules do trace the same density gas, it is quite possible that some of these regions are undergoing a chemical reaction that selectively annihilates  $\text{N}_2\text{H}^+$ .

### 3.4. B-array Observations

From the observations described above, several significant features warranted even higher resolution observations. The continuum source is seen in absorption in some species; however, it remains unresolved. CARMA’s B-array should be able to probe the region at significantly higher resolution than in our previous data. This will additionally allow us to study the velocity structure of gas near the continuum source. A velocity map of  $\text{HCO}^+$  shows an East-West velocity gradient of  $\sim 3 \text{ km s}^{-1}$ .  $\text{HCO}^+$  was chosen specifically since it does not have multiple hyperfine components which, due to blending, could pollute the velocity map, and shows absorption towards the continuum source. In addition, with these data we can see if we can resolve the individual cores of the Turner-Welch object. Previous high resolution continuum maps have shown evidence of multiple cores within the Turner-Welch object which we would expect to also see in corresponding high resolution spectral line maps. We previously choose to map the region with the C, D, and E arrays to study large scale features; with B-array alone we are able to map features that require higher spatial resolution. If we combined the B-array data with the rest, we will produce a map with a synthesized beam that is larger than the beam of the B-array data alone, and larger than some of the smallest features, obscuring them. In addition, the necessity to self-calibrate the data and issues with gain calibration (discussed in detail below) make a separate analysis more informative.

Self calibration results in several issues that need to be overcome. W3(OH)’s physical size is 0.01 pc in diameter (Kawamura & Masson 1998) which corresponds to an angular size of  $\sim 1''$ . This means that many of the longer baselines in B-array will be resolving the W3(OH) continuum source. Data from these baselines will make it difficult to self calibrate the data as it assumes a point source model for the source (or requires an accurate model of the source features which we do not have). Running self-cal on the full dataset (including resolved baselines) generates a solution that is appropriate for the data up until a UV-radius of  $130k\lambda$ , at which the solution fails. This UV-radius corresponds to a physical size of:

$$\begin{aligned} \Theta &\sim \frac{\lambda}{D} \\ &\sim \frac{\lambda}{2 * UVr} \\ &\sim 0.79'' \end{aligned}$$

Therefore running self-cal on the full dataset assuming a point source will result in large errors in the selfcal solution due to long, resolved baselines. If we “cut” the dataset so we only use the data with UV-radius  $< 130k\lambda$  for use in calculating the phase solution, we will not have this issue.

The selfcal technique fits the phase center of the data to the brightest point source in the map. Our C, D, and E array data is slightly offset in position from the pointing center, so this will result in a slight position offset between the two maps. This can be corrected for by manually fitting and entering the center position of the continuum source from our C, D, E maps, however this is not necessary since we will not be directly combining our B-array data with the rest, since the resulting maps at full angular resolution would have a very low signal-to-noise ratio.

This self-calibration technique also poses several problems with regards to flux and amplitude calibration. Several dishes primarily have long baselines, with only a few baselines that fall under our UV-radius limit of  $130k\lambda$ . While this worked well for phase calibration, the results of amplitude selfcal was very poor. Many of the amplitude gains, which should be flat and close to unity, were noisy and had many datapoints corresponding to unphysical gains that directly translates to poor image quality. The few remaining baselines also tend to have low signal to noise which further increases the problem.

In the attempt to apply correct gain calibration, several other techniques were tested to amplitude calibrate the data. We attempted to amplitude calibrate our data using the dedicated phase calibrator measurements and transferring the resulting solution to our source. This also failed, and while it produced better results than the amplitude selfcal technique described above, the high resolution, low intensity features were washed out in the final maps. This is most likely due to the gain calibrator being  $10^\circ$  from our source, far enough that the telescopes are viewing different enough atmosphere to negatively affect the calculated gains. This problem does not affect our C, D, E array data because the maximum baseline length is significantly smaller in these arrays and are not as sensitive to atmospheric fluctuations as the longer B-array baselines. Since these several technique turned out poor results, it was decided not to use amplitude (flux) calibration on the B-array data, which is not an uncommon result when using selfcal. This is another reason why we do not combine this data with our C, D, E data as we would need an accurate gain solution to provide proper weights to combine the datasets.

### 3.5. Continuum

Figure 12 represents the combined C, D, E array and B-array only continuum maps. Each map was produced using multi-frequency synthesis (MFS) on two 500 MHz windows, one in the  $N_2H^+$  band (average frequency of 91.2 GHz, not shown), and one in the CN band (average frequency of 112 GHz, shown). In Figure 12a, neither the Turner-Welch object nor W3OH are resolved. The peak flux of W3OH decreases by a factor of 2 from 91.2 GHz to 112 GHz, while the center of the Turner-Welch object increases in flux by a factor of two over the same range. In the B-array only data (Figure 12b), we resolve two individual clumps within the Turner-Welch object and slightly resolve structure within W3OH (note the off-center position of the highest level contour in Fig. 12b). This structure supports the findings of Chen et al. (2006). We additionally see the same change in relative fluxes in the B-array maps as we saw in the C, D, E array maps, over the same frequency range.

## 4. Discussion

### 4.1. W3(OH) Absorption Feature

As stated above, W3(OH) itself is a UCHII region with an embedded O7 star. Our data show that several of the molecular tracers we have observed can be seen in absorption towards this source. The nature and structure of this colder absorbing gas may be able to give us some insight into the properties of W3(OH). Figure 13 shows three spectra sampled across the continuum source in  $\text{HCO}^+$ .  $\text{HCO}^+$  was chosen for this since it does not have any hyperfine components that could cause line profile confusion.  $\text{C}^{18}\text{O}$ , while also not having any hyperfine components, was not chosen to trace this feature as it is not seen in emission or absorption towards W3(OH). The composite emission and absorption spectra are consistent with a dense, hot region (containing  $\text{HCO}^+$ ) surrounded by one or more cold, less-dense layers which also contain  $\text{HCO}^+$ . The absorption feature is evidence of cold, optically thick gas which is at a velocity of  $-46 \text{ km s}^{-1}$  and has a FWHM of  $4 \text{ km s}^{-1}$ . In looking at non-continuum subtracted spectra (Figure 13b), this absorption line is saturated and extends completely down to zero flux. This implies that this cold region is in front of the emission region and the continuum source. The absorption feature is also seen in CN and HCN, however, it is seen slightly in emission in  $\text{C}^{18}\text{O}$ . The  $\text{C}^{18}\text{O}$  emission feature is also centered at  $-46 \text{ km s}^{-1}$  and has a FWHM of  $4 \text{ km s}^{-1}$ , the same as the  $\text{HCO}^+$  absorption. It is very likely that it is from the same region, implying that the gas density is sufficient to raise the excitation temperature of the  $\text{C}^{18}\text{O}$  line above that of the brightness temperature of the continuum source so the line appears in emission, while the higher critical densities of the  $\text{HCO}^+$ , HCN, and CN transitions lead their excitation temperatures to be less than that brightness temperature, so they are seen in absorption. To note: Figure 13 is resolution limited since it is formed with C, D, and E array data and its three positions only cover an area of 1.5-2 beamwidths. This was part of the motivation to acquire B-array data as the same region would cover 5-8 beamwidths in a B-array map.

From the B-array spectra (Figure 14c), we only see  $\text{HCO}^+$  in absorption against the continuum emission. The lack of emission either means that it is being resolved out at this high spatial resolution, or that the beam is completely filled by continuum emission, so we see no emission from the sides of the beam. In either case, this means that the emission does not come from the same gas that produces the absorption. To support this, we produced spectra that only includes E-array (largest beam size, shortest baselines) in order to inspect large scale emission. The E-array data (Figure 14a) shows emission towards the continuum between  $-43 \text{ km s}^{-1}$  and  $-50 \text{ km s}^{-1}$  with a self absorption feature at  $-46 \text{ km s}^{-1}$ . This high velocity gas is not seen in  $\text{C}^{18}\text{O}$  and therefore seems to be hot, optically thin gas that is behind the continuum source.

Therefore, we propose a multi-layered model of the region around W3(OH). Behind the UCHII region is a high velocity, hot, large spatial scale, optically thin region which appears to peak in intensity towards the Turner-Welch object (and may very well be associated with it). The UCHII region is optically thin, and has a small spatial scale of about  $0.7''$  in diameter which is extremely

bright in the continuum, enough such that the narrow band 2 MHz windows are contaminated by continuum emission. In front of the continuum is a very cold, optically thick region at a velocity of  $-46 \text{ km s}^{-1}$  which we primarily see in absorption, but we see slightly in emission in  $\text{C}^{18}\text{O}$ .

## 4.2. CARMA Flux

Our maps are comprised of C, D, and E array data and do not cover the entire UV space. We do not have zero-spacing data which would be required in order to reconstruct the most accurate map of the region. The IRAM data consists of only a single pointing and its beam does not cover the full area of the CARMA maps. In order to quantify the amount of flux that could be resolved out by using CARMA, we examined the single dish data taken by Falgarone et al. (2008). Since the IRAM-30 meter telescope has a resolution of  $23''$ , we smoothed our CARMA maps to match by convolving the data with a  $23''$  Gaussian beam (Figure 15). Spectra, (16) were then extracted from the position corresponding to the IRAM-30 meter pointing center, as well as two other positions centered on the north-eastern and north-western components. According to the IRAM technical documentation (IRAM 2009), the main beam efficiency is 78% for the band that includes CN. To compare the flux values, an estimate of CARMA’s main beam efficiency is needed (White & Zauderer 2008). CARMA does not have published main beam efficiency measurements, however, it can be estimated from single-dish aperture efficiency measurements which vary from 55% to 70% depending on the individual dish. From this, we estimate that the main beam efficiency (per dish) would be  $\sim 70\text{-}80\%$ . By adopting a value of 75%, approximately the same as IRAM’s, we can directly compare the IRAM and CARMA spectra. The IRAM peak was 2.2 K, while CARMA’s was 1.4 K. This means that the peak of the CARMA spectra was at 64% of IRAM’s (the area of the CARMA spectra is 48% of the IRAM spectra). CN is also seen in strong absorption towards the central source (W3OH), however, this absorption feature is not present in any of the IRAM data. This is possible for several reasons. First, the relatively small spatial size of the absorption feature covers a small fraction of the total IRAM beam. Any measured absorption would be diluted across the entire beam and masked by the significantly greater emission. In addition, the IRAM data baseline fitting procedure could contribute to hiding the presence of a weak absorption feature.

## 4.3. $\text{N}_2\text{H}^+$ Chemical Reaction

In regions with standard CO abundances (i.e. regions that are not depleted in CO), one of the formation mechanisms of  $\text{HCO}^+$  is the destruction of  $\text{N}_2\text{H}^+$  by CO (Bergin et al. 2002; Jorgensen et al. 2004). Since there is significant support that CN remains in the gas phase at densities greater than  $10^5 \text{ cm}^{-3}$  (same as  $\text{N}_2\text{H}^+$ ) we would expect CN and  $\text{N}_2\text{H}^+$  to have a very similar spatial distribution, however, there are some regions and velocities where we would expect

to see more  $N_2H^+$  emission than we do. The particular reaction that is thought to occur is:



If we compare the regions of strong  $N_2H^+$  and  $HCO^+$  emission, we would expect them not to be coincident. In addition, we expect CO to be depleted in regions of strong  $N_2H^+$  emission, as the presence of CO would cause the formation of  $HCO^+$ , while regions with significant CO emission must be weak in  $N_2H^+$ , or the reaction between these two molecules would occur.

In the region surrounding the Turner-Welch object we can see considerable emission from both CO and  $HCO^+$ , however, there is no  $N_2H^+$  within our detection limit. This depletion of  $N_2H^+$  could be caused by the amount of  $C^{18}O$  present along this sightline. Since there is significant CN emission from this region, we would also expect to see  $N_2H^+$ . The presence of CN and the relative strengths of  $HCO^+$  and  $C^{18}O$  is significant evidence of this reaction occurring and that  $N_2H^+$  is being consumed by this reaction.

Above, we showed that there was a cold, dark region of gas towards the continuum source where  $HCO^+$  is seen in strong absorption along with CN and HCN. Discounting the contribution from the continuum source,  $C^{18}O$  is seen slightly in emission and  $N_2H^+$  is seen slightly in emission and absorption. The presence of CN absorption implies conditions where  $N_2H^+$  should also be strongly detectable. If we assume that the primary formation mechanism of  $HCO^+$  in this region is by the CO and  $N_2H^+$  chemical reaction, the relative depletion of these two chemical species in this cold dark cloud can be understood.

In regions with conditions similar to that of W3(OH), CN may be a more reliable tracer than  $N_2H^+$  to directly sample regions at high densities. However, since the strongest CN hyperfine transition has significantly weaker line emission than the strongest hyperfine transitions of  $N_2H^+$ , it would require significantly greater telescope time to achieve a comparable signal-to-noise ratio. In our case, these sets of maps show not only that this chemical reaction is occurring, but is happening most strongly both along the sightlines associated with an active star forming clump, and in a cold cloud in front of an extremely bright UCHII region.

#### 4.4. Structure of the Region Surrounding W3(OH)

Wilson et al. (1991) developed a model of the region surrounding W3(OH) based on  $C^{18}O$ ,  $C^{34}S$ , and methanol (among others). They proposed a multi-layer model of low density molecular gas surrounding a high density molecular core. This low density cooler region extends in front of W3(OH) as well. Self-absorption in their CS data supports this model. In addition, the  $v_{LSR}$  of the self-absorption was up to  $2 \text{ km s}^{-1}$  more positive than the  $v_{LSR}$  of the hotter emitting region. This implies that the cloud envelope is contracting relative to the cloud core. We see similar offsets in the E-array spectrum of  $HCO^+$  seen in Fig. 14a, however the offset appears to decrease at higher angular resolutions (Fig. 13).

We can compare the range of radial velocities at which we see molecular material. Wilson et al. (1991) data showed that  $\text{C}^{18}\text{O}$  peaks towards W3(OH) at a radial velocity of  $-46.6 \text{ km s}^{-1}$ , and peaks towards the Turner-Welch object at  $-48 \text{ km s}^{-1}$ . We see the same radial velocities in our  $\text{C}^{18}\text{O}$  data (even though our dataset was at 3mm, and theirs was at 1mm). For other species that trace related density regimes (HCN and  $\text{HCO}^+$ ), we see them peak at a velocity of  $-47 \text{ km s}^{-1}$  towards the Turner-Welch object. These species are seen strongly in absorption towards W3(OH), which makes it difficult to determine its radial velocity. These data show that the region around W3(OH) is extremely complex.

## 5. Conclusions

We mapped the  $1 \text{ arcmin}^2$  region around W3(OH) with CARMA, in which previous single-dish CN Zeeman observations detected a strong magnetic field. In determining which gas was producing the magnetic field, we were able to see the following features and make the following conclusions from their presence:

1. A strong absorption feature in  $\text{HCO}^+$ , HCN, and CN was detected towards the continuum source whose strength and line saturation implies the existence of a cold, optically thick region in front of the continuum source.
2. Comparison between CARMA spectra and spectra obtained with the IRAM-30 meter telescope (Falgarone et al. 2008) yields that CARMA detects approximately 65% of the material in this region.
3. Selective depletion of  $\text{N}_2\text{H}^+$  in comparison with the CN and  $\text{HCO}^+$  distribution indicates that  $\text{N}_2\text{H}^+$  is reacting with CO to form  $\text{HCO}^+$ . This reduces the effectiveness of  $\text{N}_2\text{H}^+$  as a high-density tracer, and favors the use of species, such as CN, in objects with similar chemical composition to W3(OH). These measurements additionally support the usefulness of CN as a high density tracer and confirms the hypothesis that CN Zeeman mapping will probe the magnetic field strength in the high density regions of molecular cloud clumps.

These conclusions lead to the result that future CN Zeeman mapping at high resolution with an interferometer is feasible and that W3(OH) is an ideal target to perform such mapping on.

## 6. Acknowledgments

Support for CARMA construction was derived from the states of California, Illinois, and Maryland, the James S. McDonnell Foundation, the Gordon and Betty Moore Foundation, the Kenneth T. and Eileen L. Norris Foundation, the University of Chicago, the Associates of the California Institute of Technology, and the National Science Foundation. Ongoing CARMA development and



operations are supported by the National Science Foundation under a cooperative agreement (NSF AST 08-38226), and by the CARMA partner universities.

## REFERENCES

- Bergin, E.A., Alves, J., Huard, T., Lada, C.J., 2002, ApJ, 570, 101
- Bock, D.C.-J., Bolatto, A.D., Hawkins, D.W., Kemball, A.J., Lamb, J.W., Plambeck, R.L., Pound, M.W., Scott, S.L., Woody, D.P., & Wright, M.C.H., “First results from CARMA: the combined array for research in millimeter-wave astronomy”, 2006, Proc. SPIE, 6267, 13
- Briggs, D.S., Schwab, F.R., Sramek, R.A., 1999, ASPC, 180, 127B
- Chen, H., Welch, W.J., Wilner, D.J., Sutton, E.C., 2006, ASPC, 356, 270
- Falgarone, E., Troland, T.H., Crutcher, R.M., Paubert, G., 2008, A&A, 487, 247
- Hachisuka, K., Brunthaler, A., Menten, K.M., Reid, M.J., Imai, H., Hagiwara, Y., Miyoshi, M., Horiuchi, S., Sasao, T., 2006, ApJ, 645, 337
- Hily-Blant, P., Walmsley, M., Pineau des Forêts, G., Flower, D., 2008, A&A, 480, 5
- Hoare, M.G., 2004, Astrophysics and Space Science, 295, 203
- <http://www.iram.es/IRAMES/mainWiki/Iram30mEfficiencies>, IRAM 30m Efficiencies
- Jorgensen, J.K., Schoeier, F.L., van Dishoeck, E.F., 2004, A&A, 416, 603
- Kawamura, J.H., Masson, C.R., 1998, ApJ, 509, 270
- Raimond, E. & Eliasson, B., 1969, ApJ, 155, 817
- Tieftrunk, A.R., Megeath, S.T., Wilson, T.L., Rayner, J.T., 1998, A&A, 336, 991
- Turner, J.L. & Welch, W.J., 1984, ApJ, 287, 81
- White, S.M., Zauderer, B.A., 2008, CARMA Memorandum Series #49, *Single-Dish Aperture Efficiency Measurements at CARMA*
- Wilner, D.J., Welch, W.J., Forster, J.R., 1995, ApJ, 449, 73
- Wilson, T.L., Johnston, K.J., Mauersberger, R., 1991, A&A, 251, 220
- Wilson, T.L., Gaume, R.A., Johnston, K.J., 1993, ApJ, 402, 230
- Wink, J.E., Duvert, G., Guilloteau, S., Güsten, R., Walmsley, C.M., Wilson, T.L., 1994, A&A, 281, 505

Wynn-Williams, C.G., Becklin, E.E., Neugebauer, G., 1972, MNRAS, 160, 1

Wyrowski, F., Hofner, P., Schilke, P., Walmsley, C.M., Wilner, D.J., Wink, J.E., 1997, A&A, 320,  
17

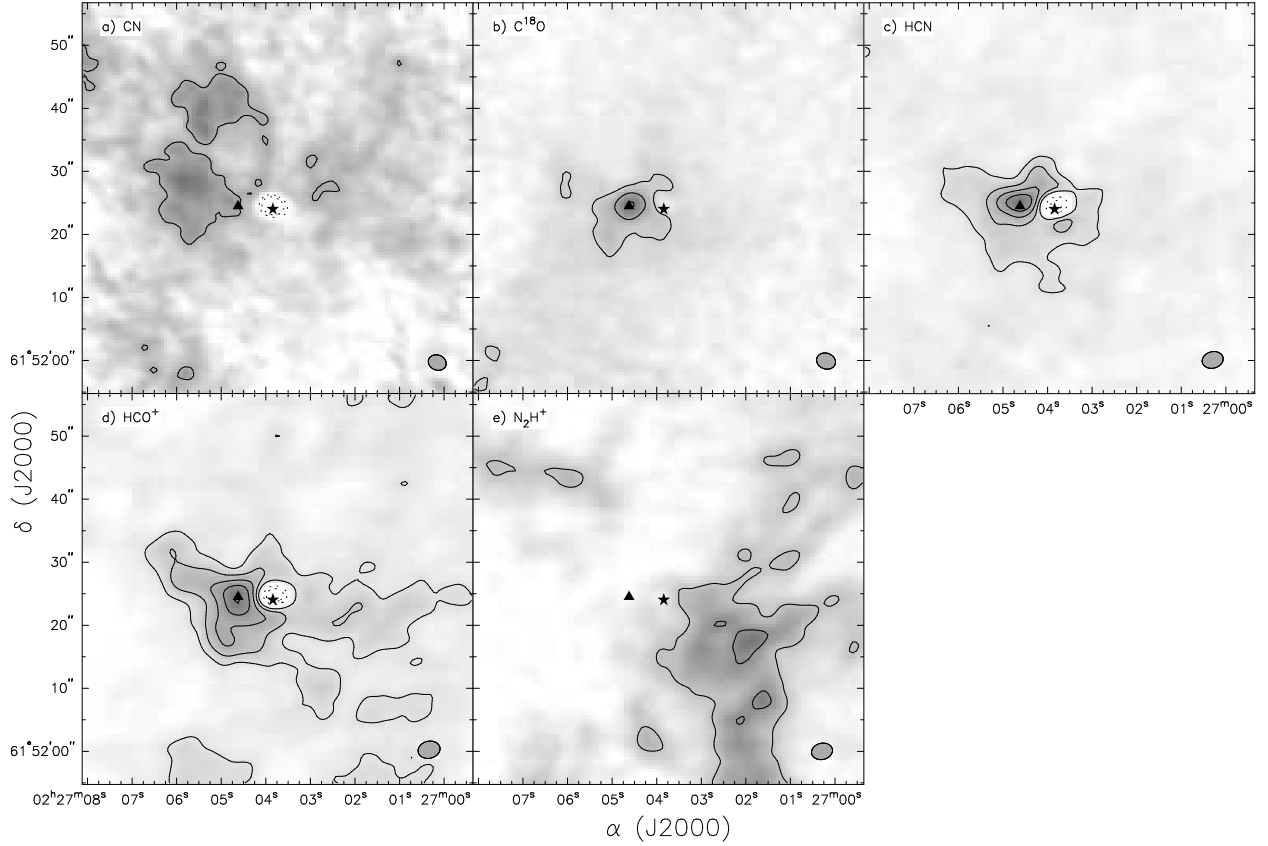


Fig. 1.— CARMA integrated line maps. (a) CN,  $2.9'' \times 2.4''$ , offline RMS =  $0.03 \text{ Jy beam}^{-1}$ , Peak intensity =  $0.29 \text{ Jy beam}^{-1}$ , Peak SNR = 9.6. (b)  $\text{C}^{18}\text{O}$ ,  $3.1'' \times 2.5''$ , offline RMS =  $0.015 \text{ Jy beam}^{-1}$ , Peak intensity =  $0.52 \text{ Jy beam}^{-1}$ , Peak SNR = 34.6. (c) HCN,  $3.4'' \times 2.6''$ , offline RMS =  $0.021 \text{ Jy beam}^{-1}$ , Peak intensity =  $0.84 \text{ Jy beam}^{-1}$ , Peak SNR = 40. (d)  $\text{HCO}^+$ ,  $3.5'' \times 2.7''$ , offline RMS =  $0.037 \text{ Jy beam}^{-1}$ , Peak intensity =  $0.86 \text{ Jy beam}^{-1}$ , Peak SNR = 23.2. (e)  $\text{N}_2\text{H}^+$ ,  $3.4'' \times 2.6''$ , offline RMS =  $0.023 \text{ Jy beam}^{-1}$ , Peak intensity =  $0.41 \text{ Jy beam}^{-1}$ , Peak SNR = 17.8. The contours are 3, 6.5, 10, 13.5, 17 times  $0.05 \text{ Jy beam}^{-1}$ . The ★ and ▲ represent the peak continuum positions of W3(OH) and the Turner-Welch object, respectively.

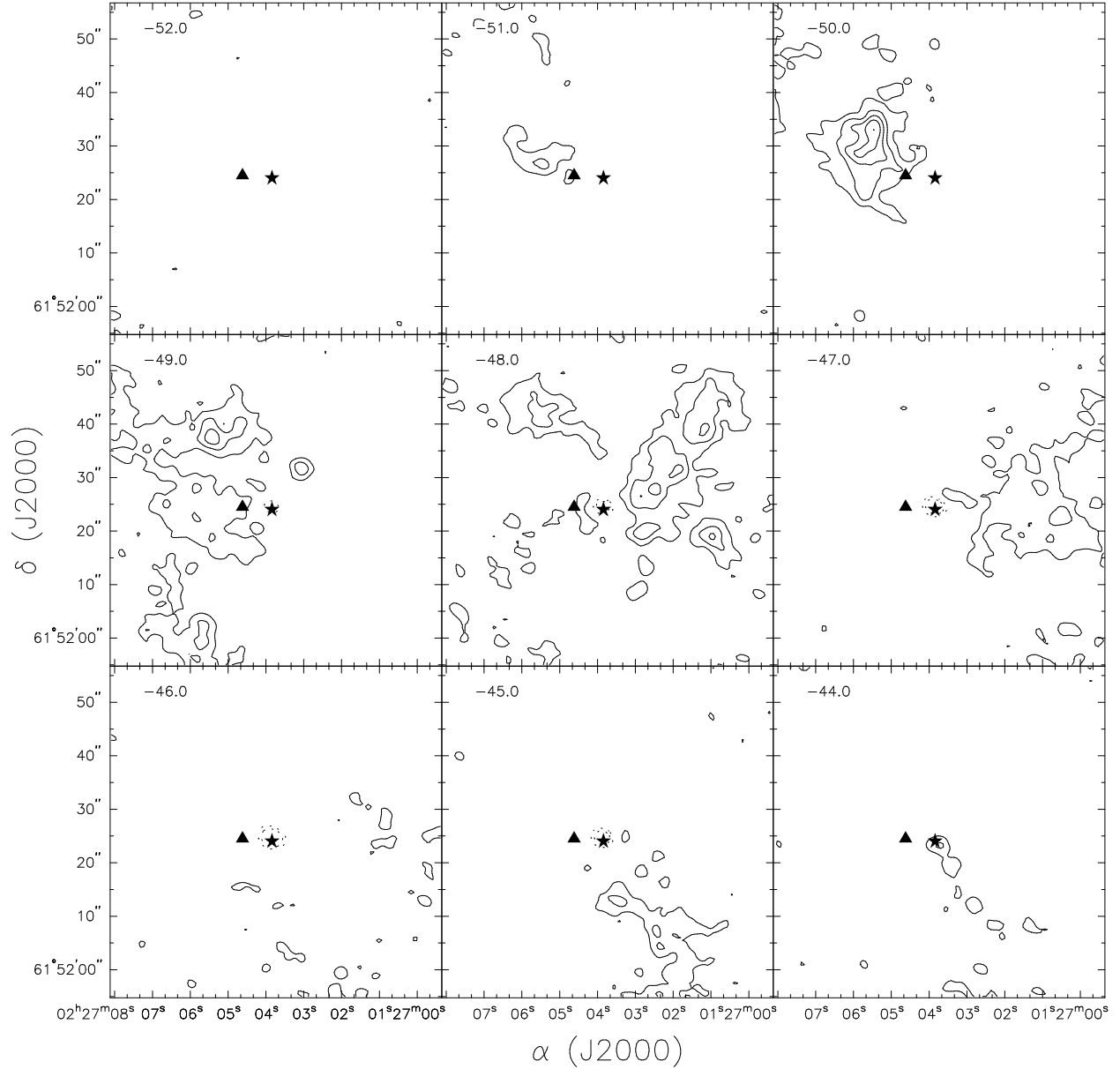


Fig. 2.— CN Channel maps, rebinned to 1 km s<sup>-1</sup> velocity increments. The velocity scale is centered on the strongest CN hyperfine component at 113.490 GHz. The spacial resolution of this map is 2.9 x 2.4 arcsec. The countour levels are -80, -40, 20, 40, 60, 80, 100 times 0.00989 Jy beam<sup>-1</sup>. The ★ and ▲ represent the peak continuum positions of W3(OH) and the Turner-Welch object, respectively.

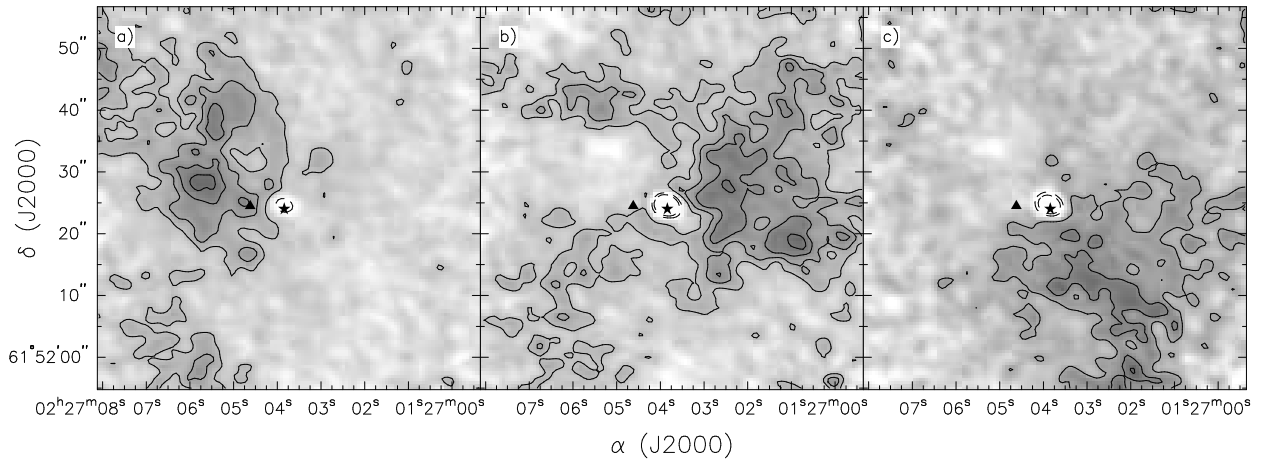


Fig. 3.— Integrated line maps of CN velocity components in W3(OH). These are the three distinct velocity components present in the CN window. Each map is averaged over the two hyperfine components present. The figure (a) is averaged from  $-52.7$  to  $-48.5$   $\text{km s}^{-1}$ , figure (b) from  $-48.2$  to  $-46.3$   $\text{km s}^{-1}$ , and figure (c) from  $-46.3$  to  $-43.1$   $\text{km s}^{-1}$ . Notable features include the dense clumps in the north-east corner of (a), and the continuum source which can be seen in absorption. The contours are 2, 4, 6, and 8 times the noise level of about  $0.03$   $\text{Jy beam}^{-1}$ . The ★ and ▲ represent the peak continuum positions of W3(OH) and the Turner-Welch object, respectively.

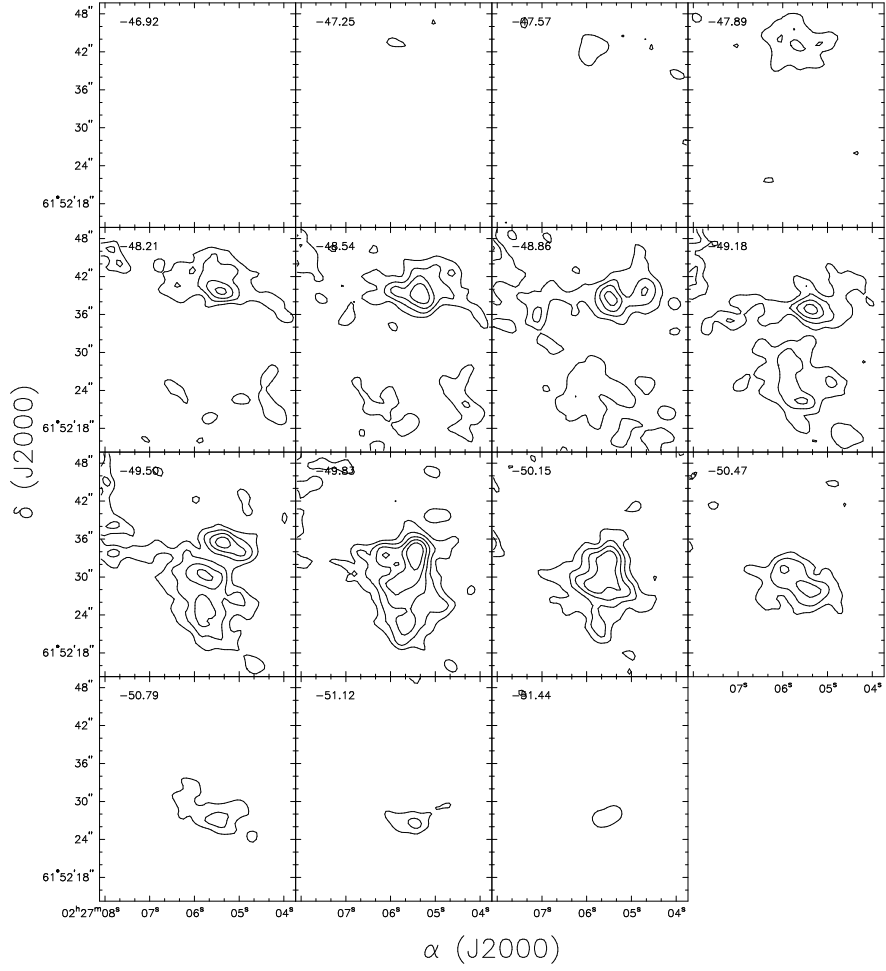


Fig. 4.— Channel maps of the CN clump in the north-eastern corner of the CN map. Displayed are 15 channels from  $-46.92 \text{ km s}^{-1}$  to  $-51.44 \text{ km s}^{-1}$ . There are two visible “lobes”, the northern one which peaks at  $-48.64 \text{ km s}^{-1}$ , and the southern one which peaks at  $-49.83 \text{ km s}^{-1}$ . The countour levels are 5, 8, 11, 14, 17 times  $0.05 \text{ Jy beam}^{-1}$ .

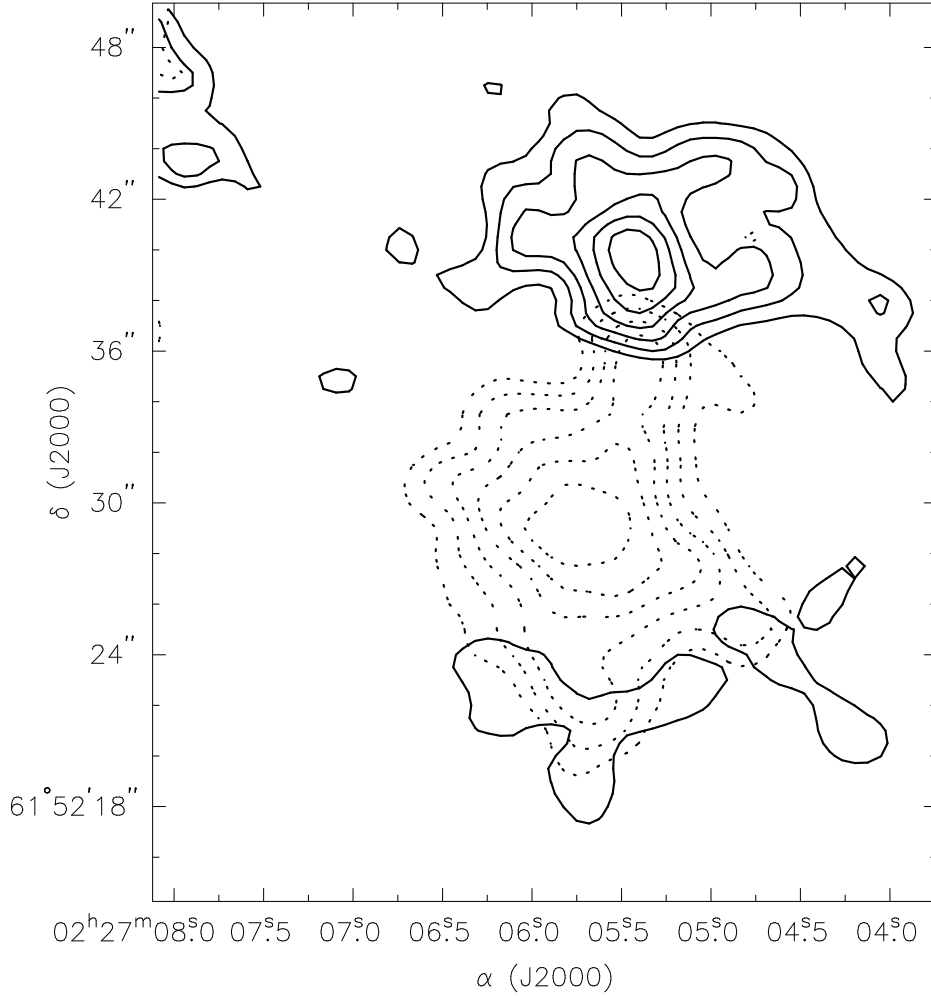


Fig. 5.— Averaged map of the two “lobes” of the outflow-like feature. The emission represented by solid contours is averaged from 6 channels between  $-47.6 \text{ km s}^{-1}$  and  $-49.2 \text{ km s}^{-1}$ . The emission represented by dotted contours is averaged from 6 channels between  $-49.2 \text{ km s}^{-1}$  and  $-50.8 \text{ km s}^{-1}$ . While this does look similar to an outflow, it could also be bulk rotation of a clump of gas. The contour levels of both objects are 4, 5, 6, 7, 8, 9 times  $0.06 \text{ Jy beam}^{-1}$ .

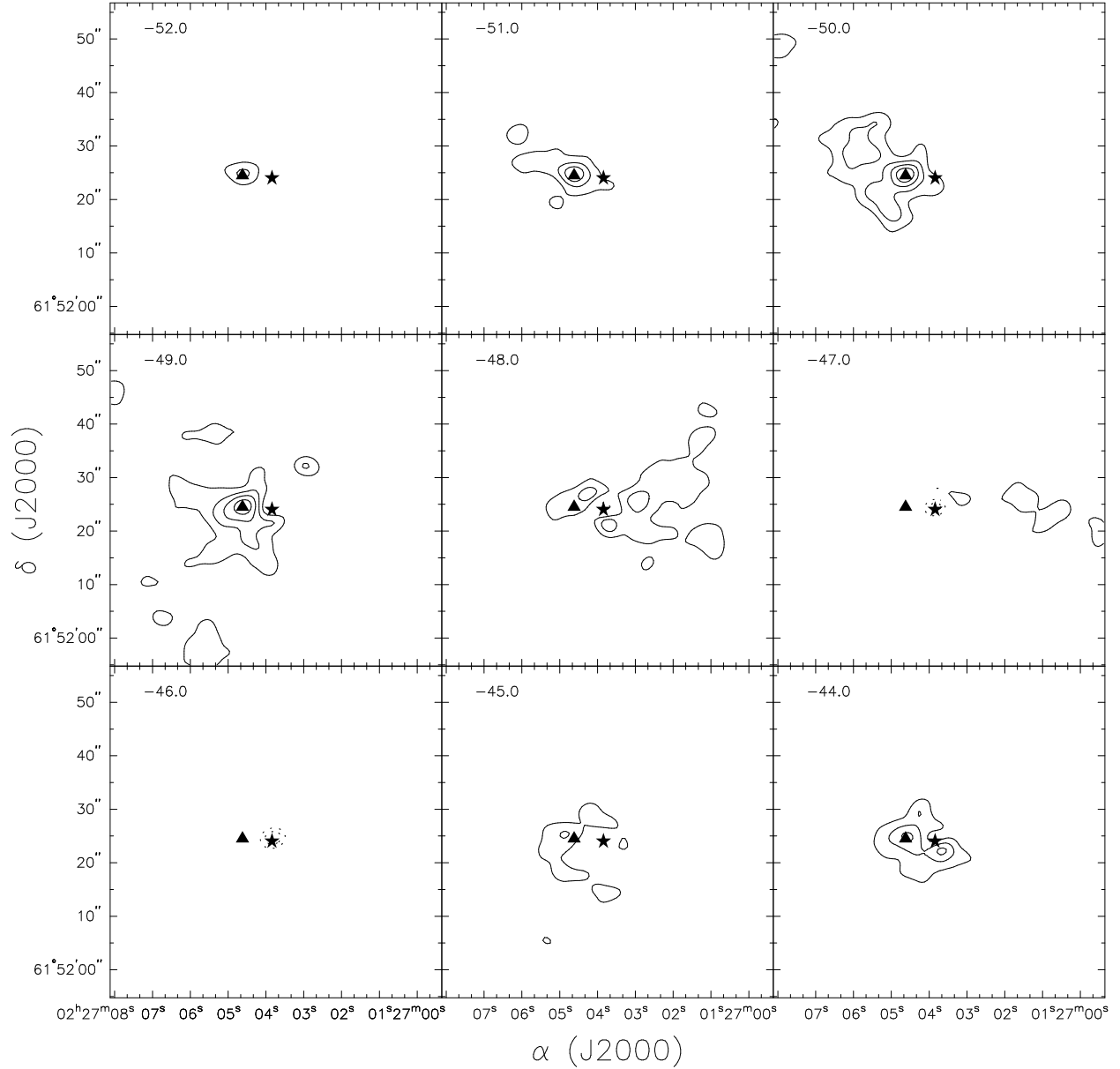


Fig. 6.— HCN Channel maps, rebinned to  $1 \text{ km s}^{-1}$  velocity increments. The velocity scale is centered on the strongest HCN hyperfine component at  $88.631 \text{ GHz}$ . The spatial resolution of this map is  $3.4 \times 2.6 \text{ arcsec}$ . The contour levels are  $-80, -40, 20, 40, 60, 80, 100$  times  $0.0287 \text{ Jy beam}^{-1}$ . The  $\star$  and  $\blacktriangle$  represent the peak continuum positions of W3(OH) and the Turner-Welch object, respectively.



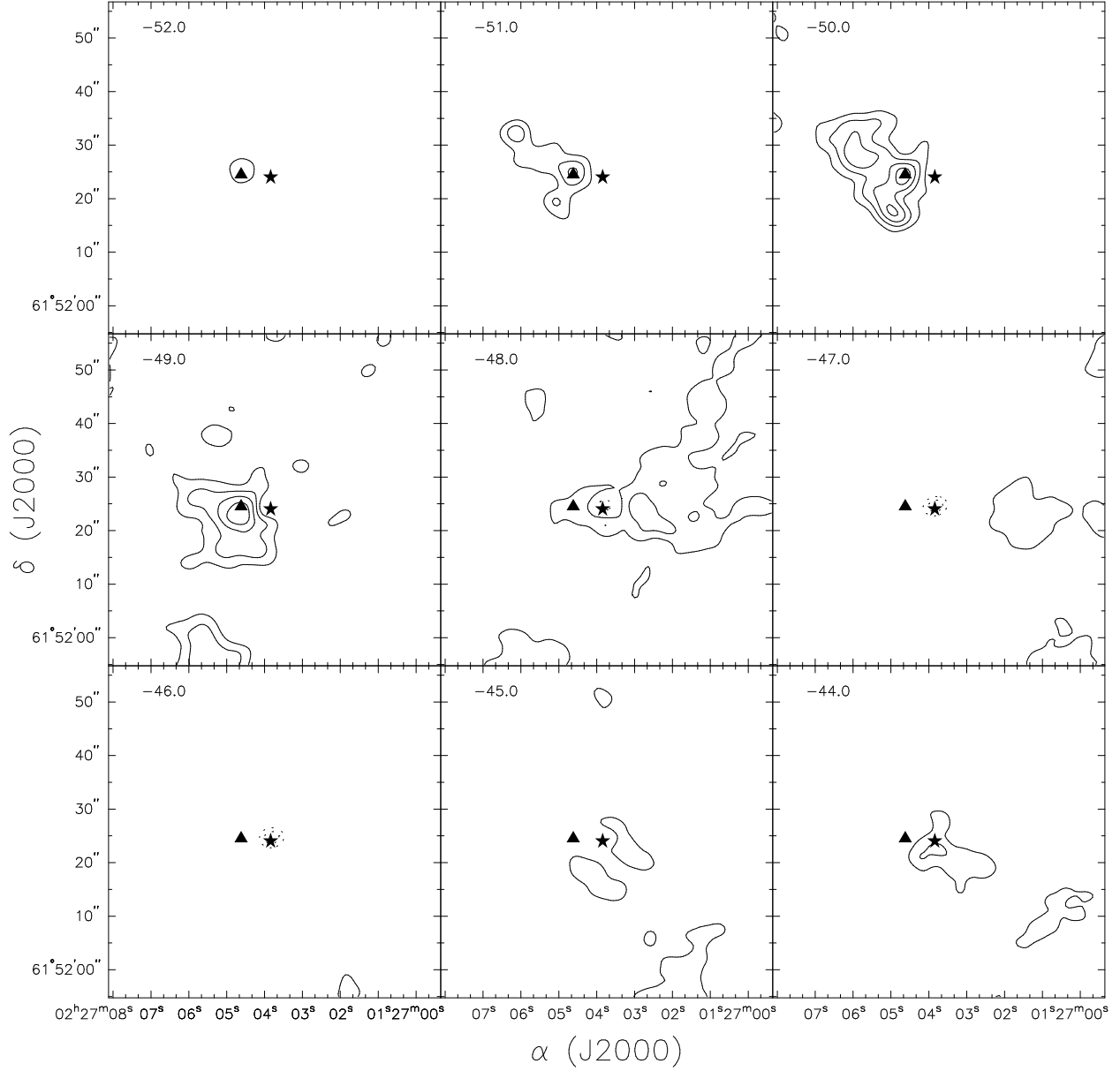


Fig. 7.—  $\text{HCO}^+$  Channel maps, rebinned to  $1 \text{ km s}^{-1}$  velocity increments. The spacial resolution of this map is  $3.5 \times 2.7$  arcsec. The contour levels are -80, -40, 20, 40, 60, 80, 100 times  $0.0296 \text{ Jy beam}^{-1}$ . The ★ and ▲ represent the peak continuum positions of W3(OH) and the Turner-Welch object, respectively.

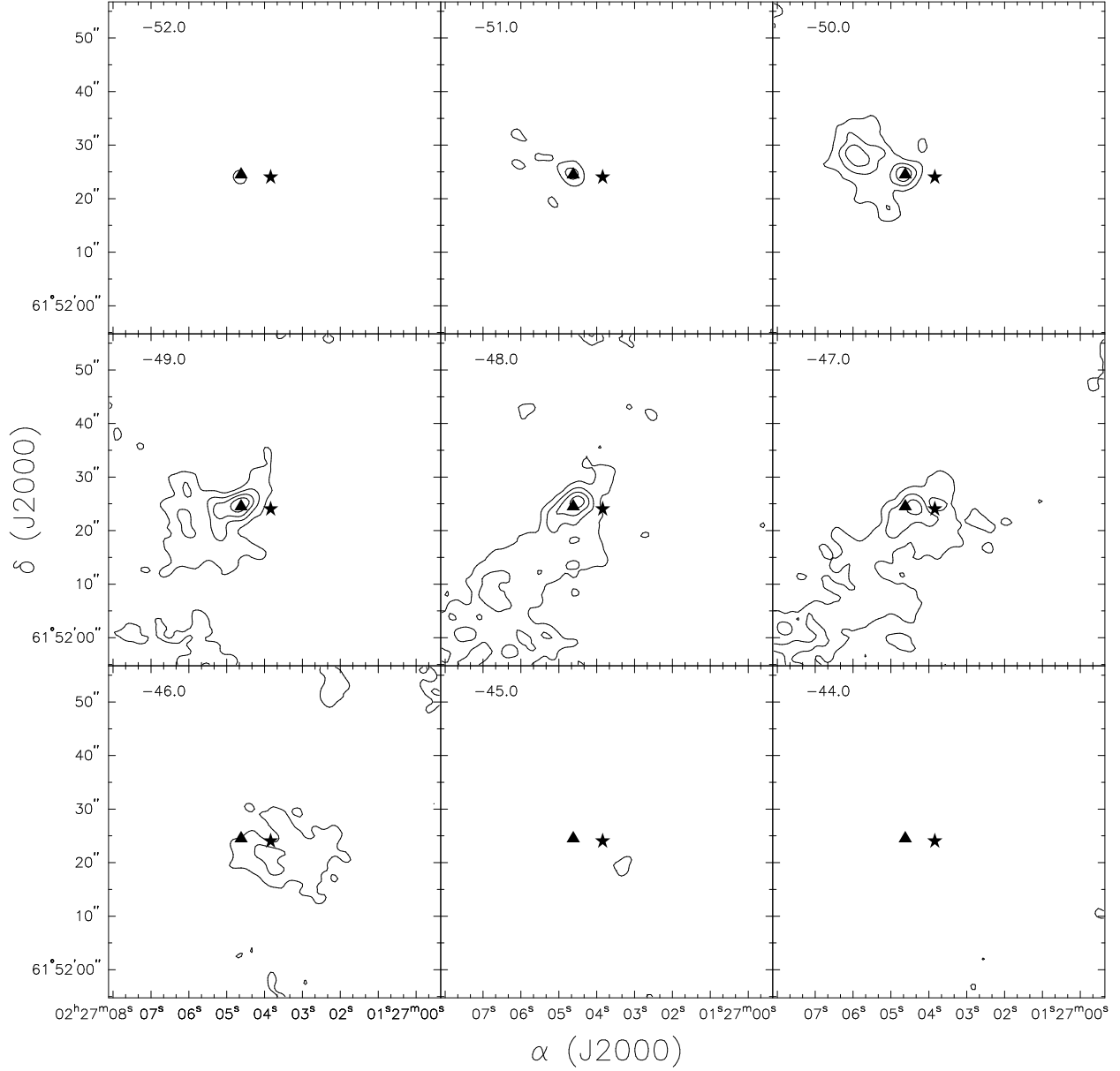


Fig. 8.—  $\text{C}^{18}\text{O}$  Channel maps, rebinned to  $1 \text{ km s}^{-1}$  velocity increments. The spacial resolution of this map is  $3.1 \times 2.5$  arcsec. The contour levels are 20, 40, 60, 80, 100 times  $0.00988 \text{ Jy beam}^{-1}$ . The  $\star$  and  $\blacktriangle$  represent the peak continuum positions of W3(OH) and the Turner-Welch object, respectively.

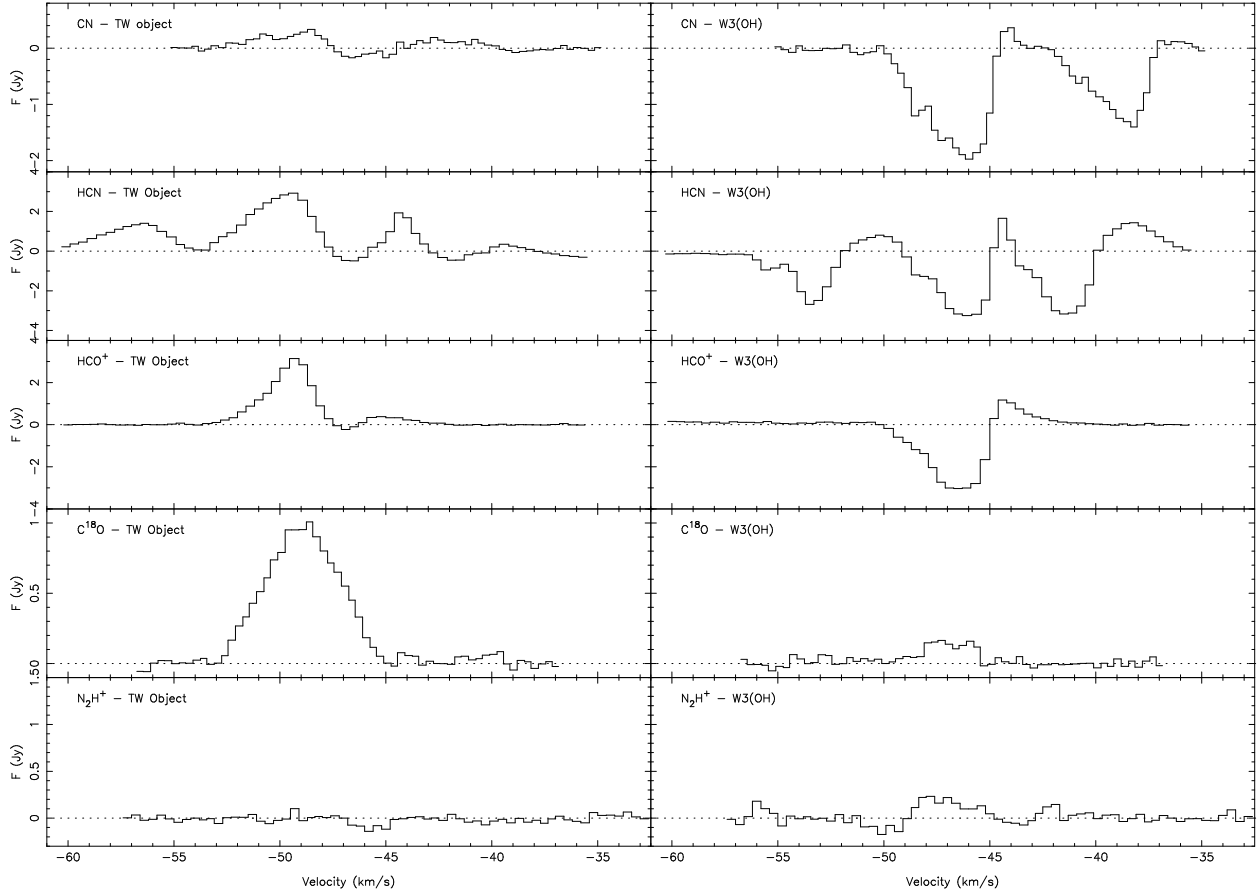


Fig. 9.— Sample spectra for each species, towards both the continuum source (W3OH) and the Turner-Welch object. For the CN, HCN, and N<sub>2</sub>H<sup>+</sup> spectra, multiple hyperfine components are present. The velocity scale for all of these corresponds to that of the strongest hyperfine component. Three of the sources can be seen in absorption towards the continuum source, while the other two have little to no emission.

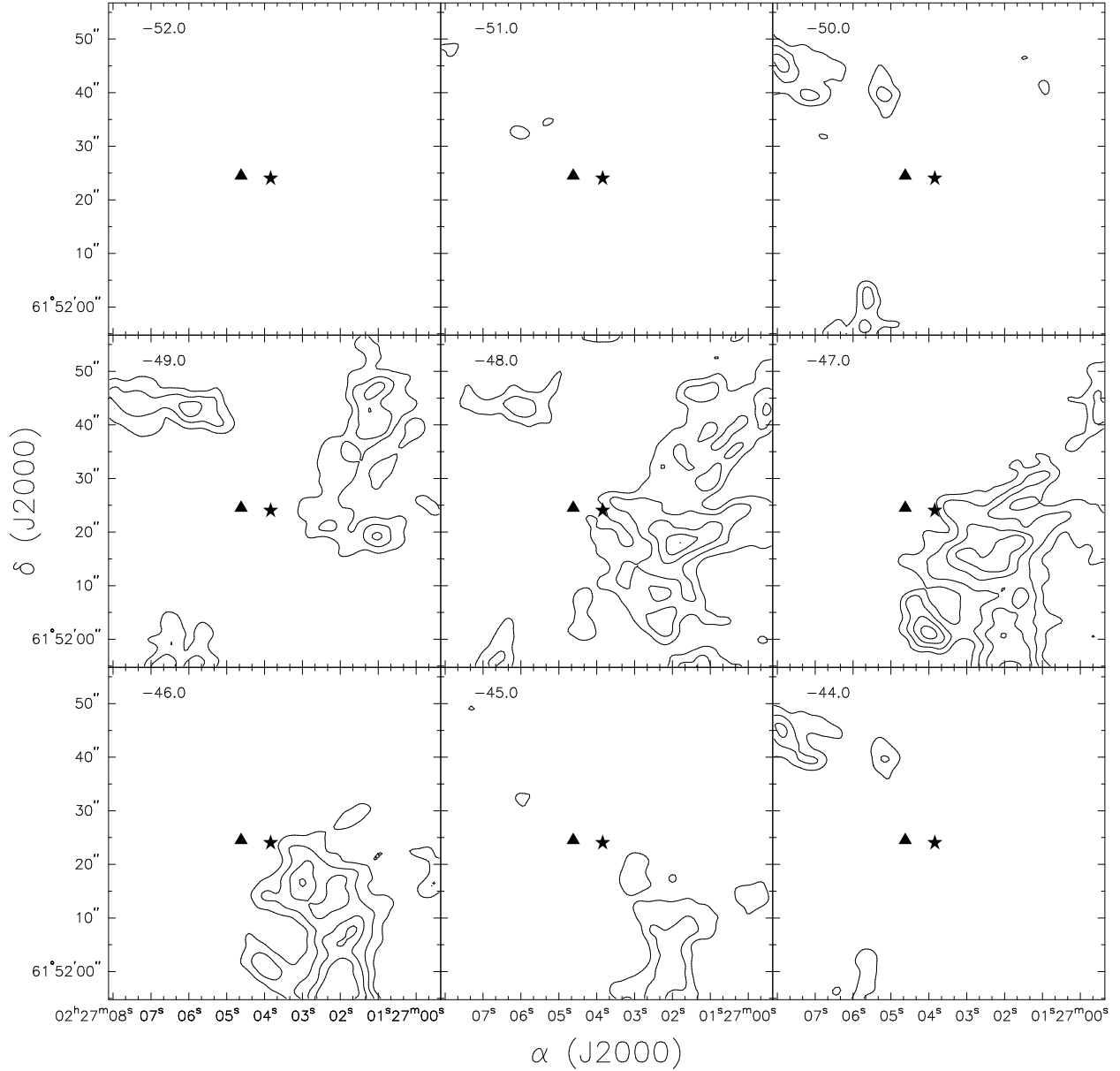


Fig. 10.—  $N_2H^+$  Channel maps, rebinned to  $1 \text{ km s}^{-1}$  velocity increments. The velocity scale is centered on the strongest CN hyperfine component at 93.17348 GHz. The spacial resolution of this map is  $3.4 \times 2.6$  arcsec. The contour levels are 20, 40, 60, 80, 100 times  $0.0129 \text{ Jy beam}^{-1}$ . The ★ and ▲ represent the peak continuum positions of W3(OH) and the Turner-Welch object, respectively.

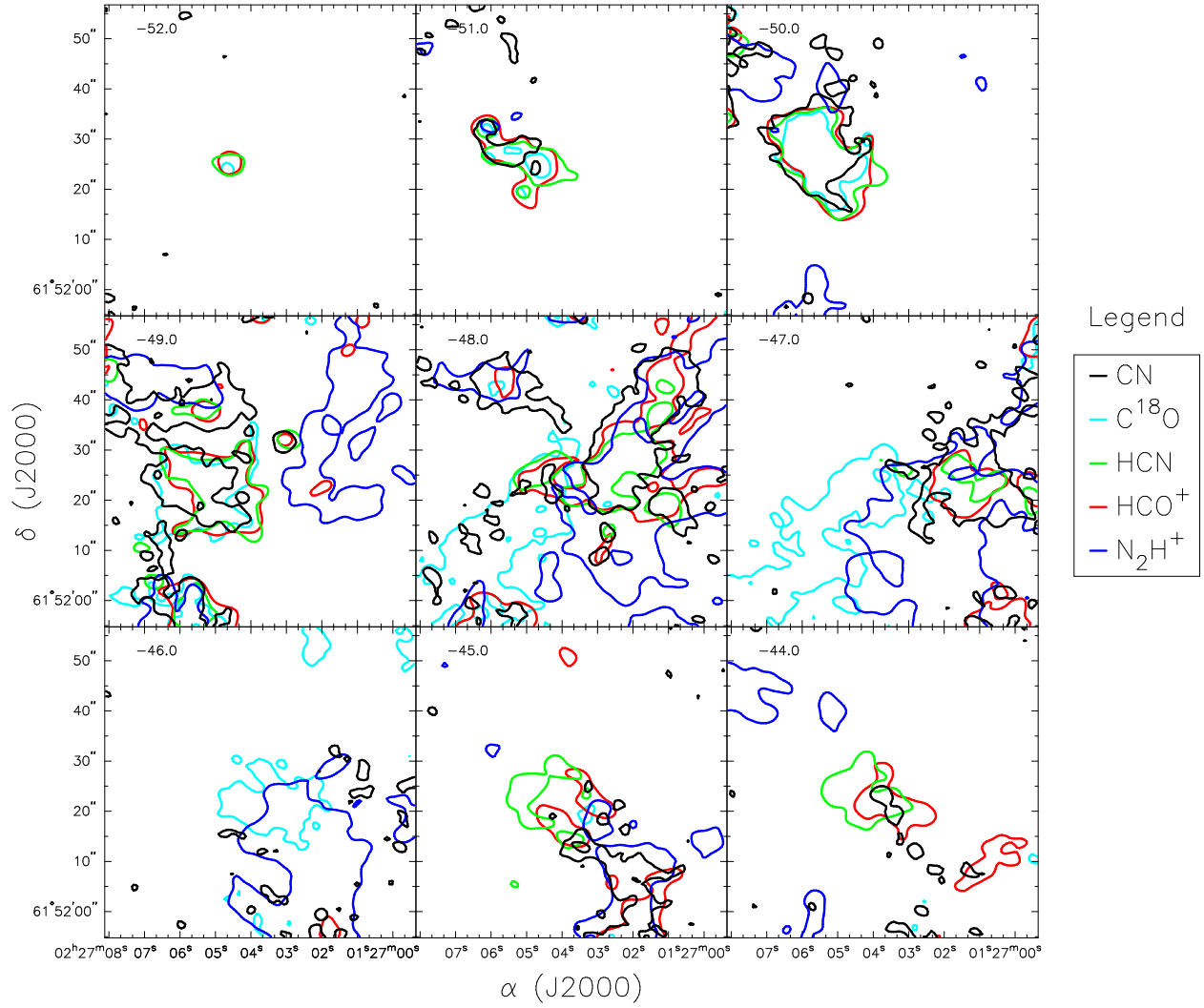


Fig. 11.— Channel map showing the 20% contour level of all the mapped species.

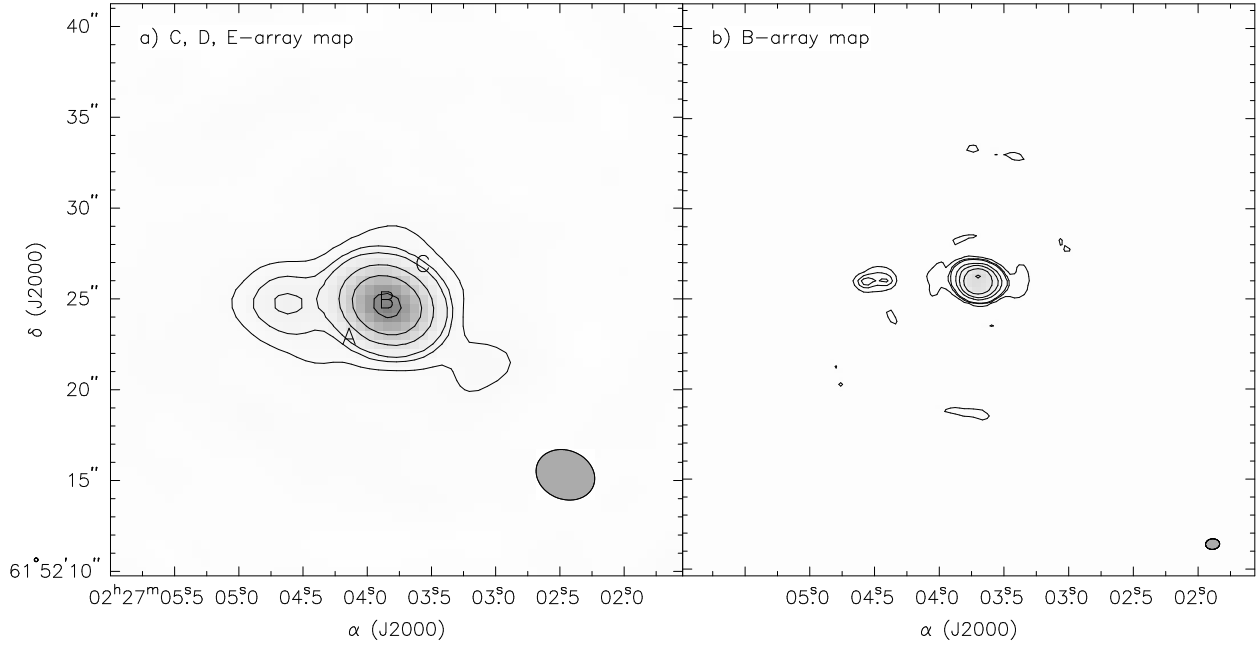


Fig. 12.— Continuum maps centered at 112 GHz. Panel a) has contour levels of 8, 16, 25, 64, 128, and 256 times  $0.009 \text{ Jy beam}^{-1}$ . Panel b) has contour levels of 3, 7, 10, 32, 64, 128, and 256 times  $0.003 \text{ Jy beam}^{-1}$ . The range in contour levels are to show the dynamic range of features visible in these maps. a) has a beam size of  $3.3'' \times 2.7''$ , b) has a beam size of  $0.77'' \times 0.59''$ . Positions A-C marked in the first panel represent the positions of spectra in Figure 13.

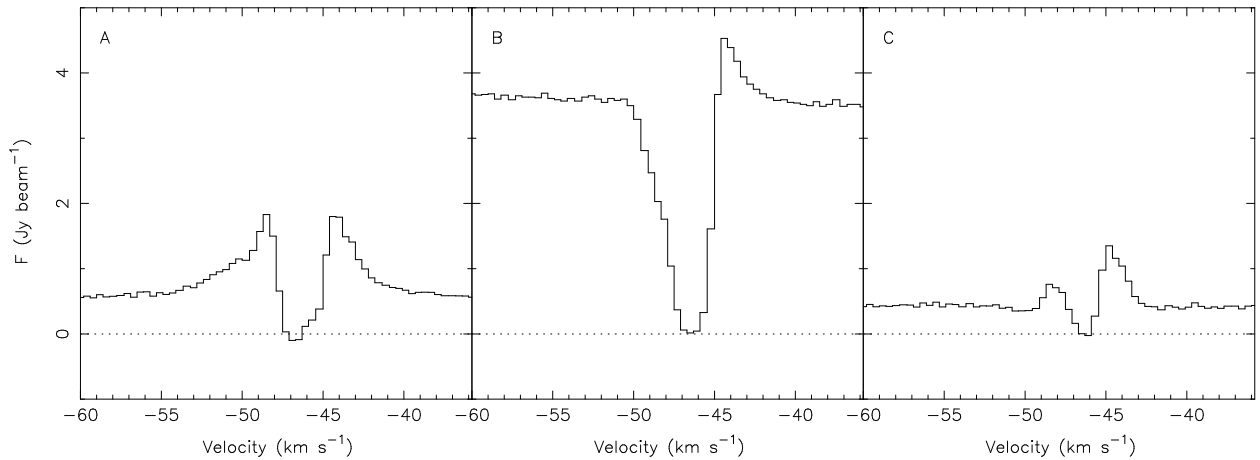


Fig. 13.— Panels A-C are  $\text{HCO}^+$  spectra of W3(OH) at three positions with no continuum subtraction. This shows the change in emission and absorption spectra in  $\text{HCO}^+$  across the W3(OH) Ultra-Compact HII region. Panel A is  $2''$  SE of the W3(OH) center position, and Panel C is  $2''$  NW of the W3(OH) center position. The positions of spectra A-C are marked on Figure 12a for reference.

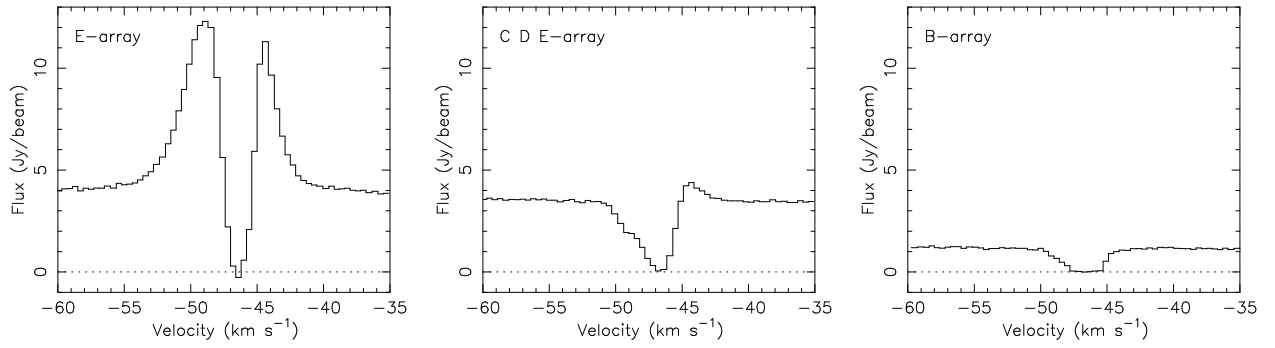


Fig. 14.— Comparison between spectra towards the center of the continuum source in a) E-array only, b) combined C, D, E array maps, and c) B-array only. In all three instances, the spectra are seen in absorption at the same velocities and with roughly the same linewidth which supports a model of a cold dark, optically thick cloud in front of the continuum source and emission regions in our map.

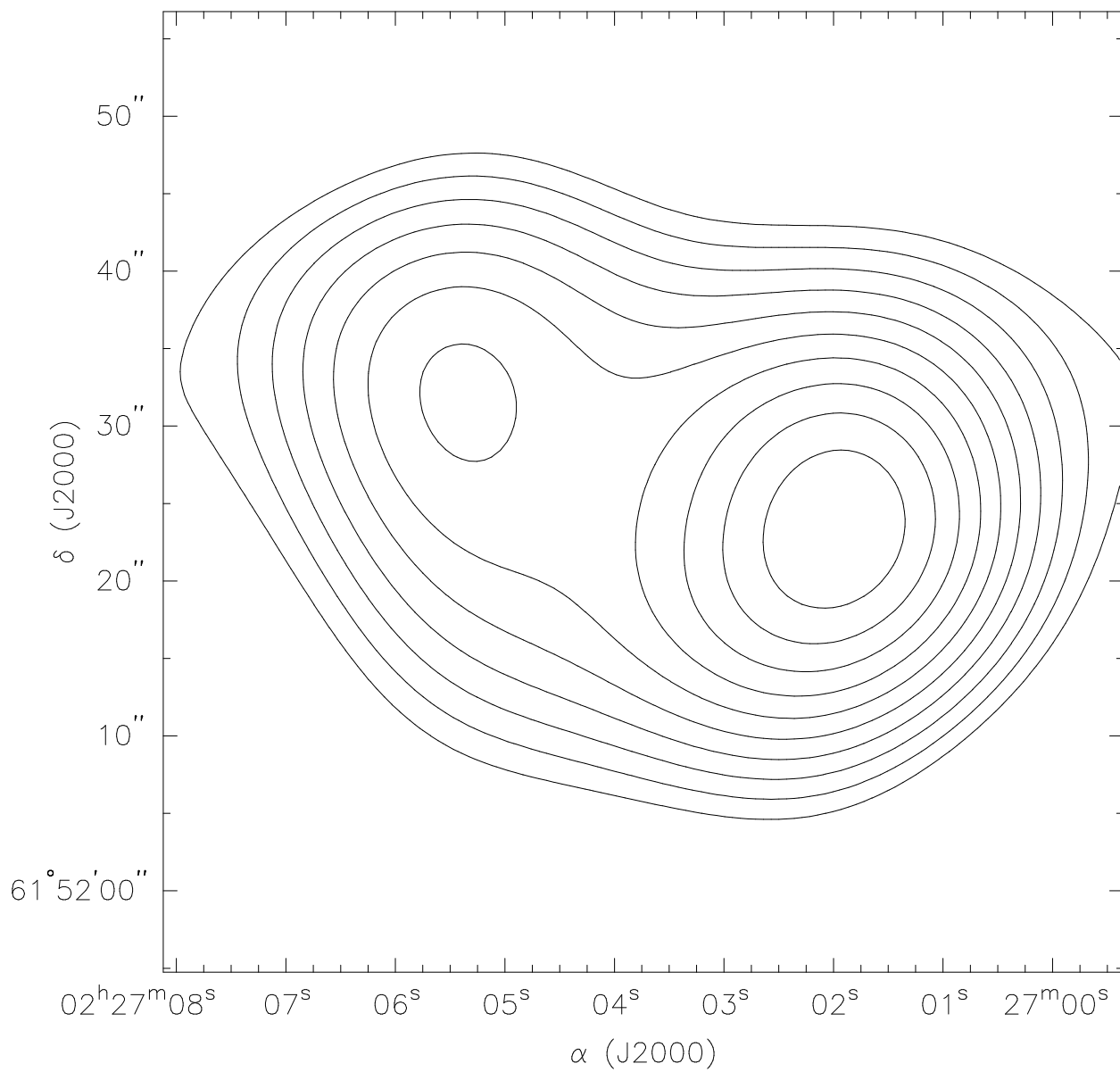


Fig. 15.— Smoothed CARMA CN map to the same resolution as the IRAM measurements ( $23''$ ). This was produced by convolving a  $23''$  Gaussian beam with the integrated line map seen in Fig. 1. The contour levels are in increments of  $0.158 \text{ Jy beam}^{-1}$  from  $1.89 \text{ Jy beam}^{-1}$  to  $3.47 \text{ Jy beam}^{-1}$ .



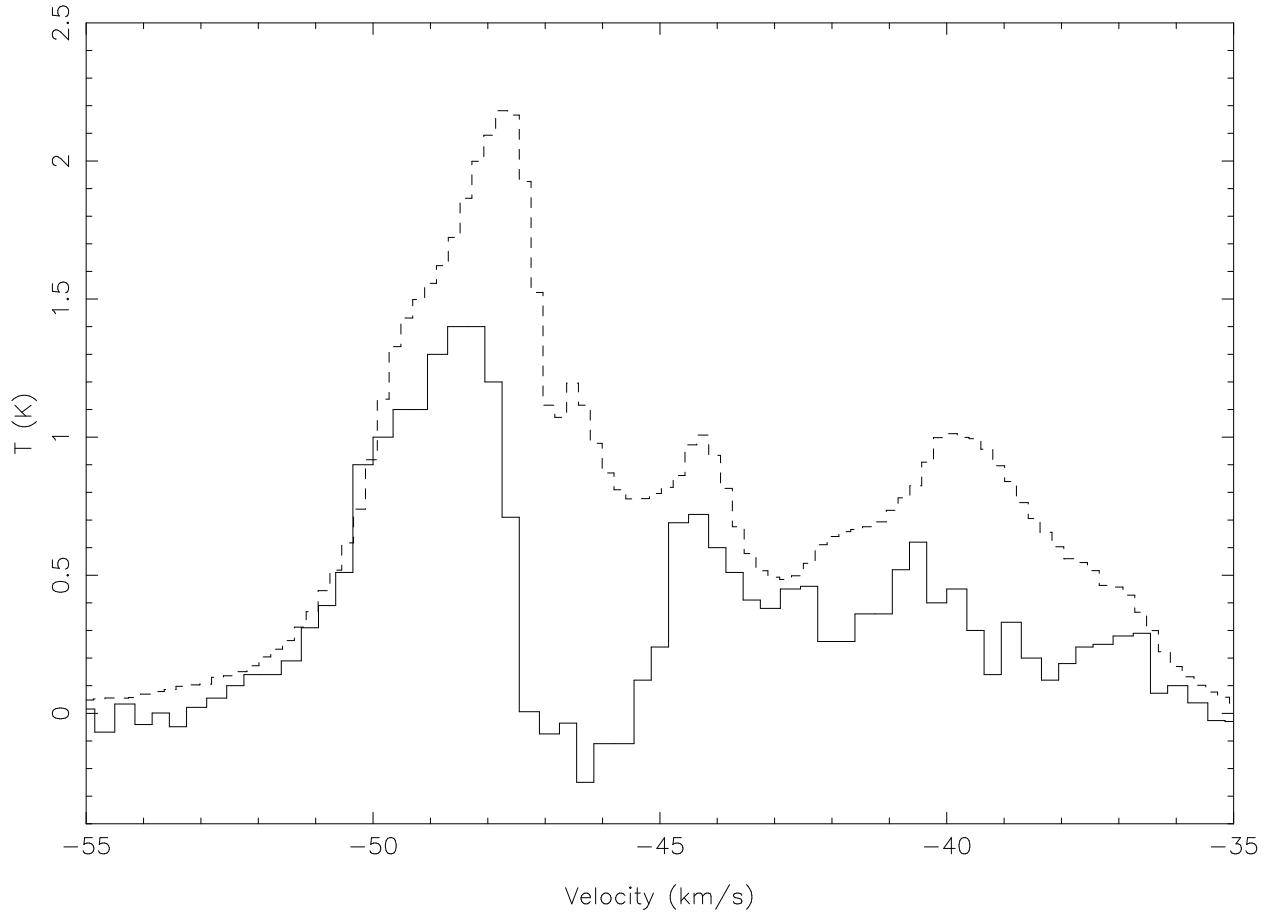


Fig. 16.— CARMA spectrum overlaid with the IRAM spectrum at a point near the IRAM pointing center. Note that there are two CN hyperfine lines in these spectra, separated by about  $8 \text{ km s}^{-1}$ . The velocity scale is for the stronger hyperfine line (at  $\sim 48 \text{ km s}^{-1}$ ). The intensity scale is estimated by comparing the main beam efficiencies of IRAM and CARMA, however, there is an inherent 20% error in the CARMA flux measurements. From this, we estimated that CARMA resolves  $\sim 65\%$  of the CN emission within the IRAM beam.